A MORPHING-BASED APPROACH FOR THE VERIFICATION OF PRECIPITATION FORECASTS

A Dissertation

by

FAN HAN

Submitted to the Office of Graduate and Professional Studies of
Texas A&M University
in partial fulfillment of the requirements for the degree of

MASTER OF SCIENCE

Chair of Committee,	Istvan Szunyogh
Committee Members,	Ping Chang
	Mikyoung Jun
	Ramalingam Saravanan
Head of Department,	Ping Yang

December 2014

Major Subject: Atmospheric Sciences

ABSTRACT

This thesis described a morphing-based precipitation verification strategy inspired by Keil and Craig. This strategy is based on an optical flow algorithm to morph the image (field) of the forecast precipitation into an image that resembles the image (field) of the observed (analyzed) precipitation. This method treats the precipitation as a passive scalar and carries out the morphing by computing a vector field, called the optical flow, which is then used to advect the original forecast precipitation field. The information provided by the optical flow and the morphed image of the forecast precipitation field is used to define the measures of the displacement error and residual error.

There are two novel aspects of our strategy. First, it imposes a constrain on the morphing process in order to prevent the over-convergence of pixels during morphing to a few locations of large errors. Second, it uses a new definition of the displacement error and provides a new interpretation of the other error terms.

By applying the new morphing-based precipitation strategy to a schematic idealized example and a real hurricane example, we demonstrate that the constrain imposed largely reduces the risk of over-convergence and the error measures we derive from the morphing process accurately measure the corresponding error components.

ACKNOWLEDGEMENTS

I would like to express my appreciation to my advisor, Dr. Istvan Szunyogh, for his patience, encouragement and continual inspiration through the whole process of the master thesis. This thesis would not have been possible without the immense support of my advisor.

Also, I would like to thank my thesis committee members: Dr. Chang Ping, Dr. Mikyoung Jun and Dr. Ramalingam Saravanan, for their insightful comments.

My sincere thanks also goes to Dr. Gyorgyi Gyarmati for her help with computer-related work, and Guanglin Tang, for his advices on how to write computer programs.

I want to acknowledge the financial, academic and technical support of Texas A&M University and the funding source: BP/The Gulf of Mexico Research Initiative. I also thank the professors and staff members at Department of Atmospheric Science for their support and assistance since the start of my master's study in 2012.

TABLE OF CONTENTS

Page

LIST OF FIGURES

LIST OF TABLES

TABLE Page

1. INTRODUCTION

Increasing model resolution has lead to qualitatively more realistic precipitation forecasts [e.g., 3, 15, 16, 17]. The greater qualitative realism of the forecast precipitation fields, however, does not necessarily translates into quantitatively more accurate forecasts. In fact, studies using traditional precipitation verification metrics have failed to show consistent improvements with increasing model resolution [3, 12]. This result may be due to the limitations of the traditional, point-to-point verification techniques rather than to the lack of forecast improvements. In particular, such techniques

indicate a large error in a situation where a generally well predicted precipitation event of high spatial variability is slightly misplaced. This problem has motivated the search for verification techniques that can separate the forecast errors due to the displacement of the precipitation field from those due to other sources. The collection of errors that fall into the latter group is called the intensity error.

Several techniques have been proposed in the literature to separate the displacement error from the intensity error [e.g., 2, 4, 5, 6]. One approach is to identify distinct spatial patterns of precipitation as *objects* and comparing the properties of matching objects in the forecasts and the analyses (observations). The distance in space between the matched objects measures the displacement error, while the differences between the objects are the intensity error.

Our focus is on the approach proposed by Keil and Craig [8, 9], which employs an *optical flow method* to morph the image (field) of the forecast precipitation into an image that resembles the image (field) of the observed (analyzed) precipitation as closely as possible. This method treats the precipitation as a passive scalar and

carries out the morphing by computing a vector field, called the *optical flow,* which is then used to advect the original forecast precipitation field. The information provided by the optical flow and the morphed image of the forecast precipitation field can be used to define the measures of the displacement and the intensity error.

There are two novel aspects of our study. First, we demonstrate that morphing has a tendency to move precipitation into a highly localized region around the location of the largest forecast error, leading to the complete removal of precipitation from the other regions, including those where precipitation is observed and reasonably well predicted by un-morphed (original) forecast. We show that imposing a simple constraint on the morphing process can greatly reduce this problem. Second, we define the displacement and the intensity error differently than Keil and Craig [9], because we believe that our measures interpret the information provided by the optical flow and the morphed image about the forecast error more accurately.

The structure of the thesis is as follows. Section 2 describes the pyramid matching algorithm and our modifications to the algorithm, while Section 3 introduces our definitions of the the error components. Section 4 briefly describes the regional coupled atmosphere ocean model that we use to produce high-resolution precipitation forecasts and the data sets that we use for the verification of those forecasts. Section 5 investigates the behavior of the error measures by an analysis of the verification results. Section 6 offers our conclusions.

2. THE PYRAMID MATCHING ALGORITHM

2.1 The original algorithm

The optical flow method employed by Keil and Craig [8, 9] is a *pyramid matching algorithm*. The name reflects the property of the algorithm that it morphs the image of the precipitation iteratively, matching the images at increasingly higher resolution. Both the forecast and the analyzed fields are treated as the collections of elementary parcels (pixels). When the data are provided on a grid, the value of the precipitation for a pixel can be obtained by averaging the grid point values that fall within the area covered by the pixel. In addition, it is always the forecast data that is remapped to match the structure of the verifying analysis (observation).

Before providing a step-by-step description of the algorithm, we introduce our notations and provide a synopsis of the algorithm. The symbol $\mu_{i,j}$ denotes the elementary parcel located at position (i, j) before morphing, where $i = 1, 2, \ldots, N$ and $j = 1, 2, \ldots, N$ are the zonal and the meridional indexes of location, respectively. To simplify notation, we assume that the elementary parcels are d-by-d squares. In addition, we denote the forecast and observed precipitation for $\mu_{i,j}$ by $P^f_{i,j}$ and $P^o_{i,j}$, respectively. The algorithm calculates the *displacement vector* $d\mathbf{X}_{i,j} = (di, dj)_{i,j}$, which points from the location (i, j) of each parcel of the original forecast image to the new location $(i + di, j + dj)$ of the parcel in the morphed forecast image. The passive scalar $P^f_{i,j}$ is transported from (i, j) to $(i+di, j+dj)$ by the elementary parcel. When multiple elementary parcels arrive at the same location, the new value of the precipitation is obtained by a summation of the precipitation for all parcels that arrive at that location. The vector field $d\mathbf{X}_{i,j}$, $i = 1, 2, \ldots, N$ and $j = 1, 2, \ldots, N$, is the *optical flow*. In the atmospheric sciences, the pyramid matching algorithm was

first used for the computation of motion vectors from satellite images of clouds [18]. In that application, $P^f_{i,j}$ is defined by the intensity, or the brightness temperature of the pixels of the satellite images.

The most important parameter of the algorithm is called the *sub-sampling parameter*. For a particular value F of the subsampling parameter, the optical flow and the related morphed image is computed in the following steps:

1. Both the images of the forecast and the analyzed precipitation are coarse grained by averaging $P_{i,j}$ for $2^F \times 2^F$ elementary parcels. That is, the coarse-grained fields are covered by $(N/2^F) \times (N/2^F)$ coarse-grained parcels, $\mu^{(F)}_{i,j}$, $i = 1, 2, \ldots, N/2^F$ and $j = 1, 2, \ldots, N/2^F$, of size $2^F d$-by-$2^F d$. The precipitation for the coarse grained parcels is computed by averaging the values for the elementary parcels that form the coarse grained parcel. The precipitation for the coarse grained parcels is denoted by $P^{f(F)}_{i,j}$ for the forecast field and by $P^{a(F)}_{i,j}$ for the analyzed (observed) field. Here, $i = 1, 2, \ldots, N/2^F$ and $j = 1, 2, \ldots, N/2^F$.

2. An intermediate optical flow is computed by

   (a) shifting the position of the parcels of the coarse grained forecast image by $0, \pm 2^F d$ in both zonal and meridional directions;

   (b) computing

   $$D^{(F)}_{i,j} = \sum_{i'=i-I}^{i+I} \sum_{j'=j-J}^{j+J} \left(P^{f(F)}_{i',j'} - P^{a(F)}_{i',j'} \right)^2, \tag{2.1}$$

   for each of the 9 shifted positions, where (i, j) is the position of the coarse grained parcel $\mu_{i,j}$, and I and J define the size of the local region centered at (i, j), in which the coarse grained images are compared to determine $d\mathbf{X}^{(F)}_{i,j}$;

(c) defining the components of $d\mathbf{X}_{i,j}^{(F)}$ by the values of $di = i' - i$ and $dj = j' - j$ that minimize $D_{i,j}^{(F)}$; and

(d) interpolating the components of $d\mathbf{X}_{i,j}^{(F)}$ to the elementary parcels of the original full resolution image.

3. The interpolated intermediate optical flow is used to obtain an intermediate (full resolution) morphed forecast image from the the original full resolution (not coarse grained) forecast image;

4. The intermediate image is coarse grained by averaging the precipitation for $2^{F-1} \times 2^{F-1}$ elementary parcels and the procedures of Step 2 applied to obtain the next intermediate optical flow and intermediate morphed forecast image;

5. Steps 2-4 are repeated until step 3 is completed at full resolution.

The final iteration of the algorithm produces the final optical flow and the final morphed image. The number of the levels of the pyramid is $F + 1$.

Because parcels can merge when they arrive at the same location, the optical flow is not a simple translational flow. Thinking of the elementary parcels as infinitesimal parcels, the aforementioned property can be stated by saying that the optical flow is not divergence-free. This behavior of the algorithm can be advantageous in situations, where the model does not represent some of the small-scale divergent processes correctly: the morphing can introduce the related observed structures into the forecasts, such allowing for a more realistic comparison of the overall structure of the precipitation fields.

In some situations, however, morphing can lead to a convergence of the forecast precipitation that is not due to convergence in nature and the lack thereof in the model. This undesirable convergence is an artifact of the morphing process and it

occurs when morphing tries to correct for a large local error in the intensity forecast by moving in precipitation from parts of the surrounding area where precipitation is both observed and generally well predicted. An example for such a situation is shown in Fig 2.1. Panel a) shows the original forecast field, panel b) the verifying analysis, panel c) the displacement vector, and panel d) the morphed forecast field. A comparison of panel b) and d) shows that morphing shifts all precipitation from the Gulf of Mexico to the east over land, where the observed precipitation is the heaviest, but no precipitation is forecast. Such a shift would be acceptable, if no precipitation was observed in the part of the Gulf of Mexico from which the forecast precipitation was removed. While a comparison of panels a) and b), or equivalently, the investigation of the vector field in panel c), provides some useful information about the position error, a comparison of panels b) and d) would lead to falls conclusion about the local intensity errors.

2.2 The modification to the algorithm

We show that the aforementioned problem with the algorithm can be eliminated by a simple modification of the algorithm. This modification requires the introduction of the notation of a *local hit rate*, which we call local, because we define it for each coarse-grained parcel $\mu_{i,j}^{(F)}$ of a pyramid level. To define the local hit rate $h\left(mu_{i,j}^{(F)}\right)$, we introduce the notations $a\left(\mu_{i,j}^{(F)}\right)$ for the number of elementary parcel in which the presence of precipitation is correctly predicted and $c\left(\mu_{i,j}^{(F)}\right)$ for the number of elementary parcels in which the forecast fails to predict the presence of precipitation. Note that $a\left(\mu_{i,j}^{(F)}\right) + c\left(\mu_{i,j}^{(F)}\right)$ is the total number of elementary parcels in which precipitation is observed within the coarse-grained parcel $\mu_{i,j}^{(F)}$. The

local hit rate is defined by

$$h\left(\mu_{i,j}^{(F)}\right) = \begin{cases} \frac{a\left(\mu_{i,j}^{(F)}\right)}{a\left(\mu_{i,j}^{(F)}\right)+c\left(\mu_{i,j}^{(F)}\right)}, & \text{if } P_{i,j}^{a(F)} > 0, \\ 0, & \text{if } P_{i,j}^{a(F)} = 0. \end{cases} \tag{2.2}$$

According to this definition, $1 \geq h\left(\mu_{i,j}^{(F)}\right) \geq 0$. The local hit rate for $P_{i,j}^{a(F)} > 0$ can be interpreted as an estimate of the (conditional) probability of the predicted and the observed precipitation patterns within $\mu_{i,j}^{(F)}$ being related given the condition that precipitation is observed within $\mu_{i,j}^{(F)}$. If this probability is high, shifting the corse-grained parcel is not justified. This argument motivates us to make the modification to the morphing algorithm that during the computation of the intermediate flow, the position of the parcel $\mu_{i,j}^{(F)}$ is shifted only if $h\left(\mu_{i,j}^{(F)}\right) < \epsilon$, where $1 > \varepsilon > 0$ is a prescribed threshold value.

The effect of our suggested modification to the algorithm on the case shown in Fig 2.1 is illustrated by panels e) and f). Comparing panels c) and e), it can be seen that the modification eliminates the complete removal of the forecast precipitation from the Gulf of Mexico. The morphed precipitation field of panel f) correctly reflects that significant precipitation is observed both over both the Gulf of Mexico and Florida. The morphed field of panel f), however, still has the undesirable feature of over-convergence of the precipitation into the two highly localized regions of largest local forecast errors.

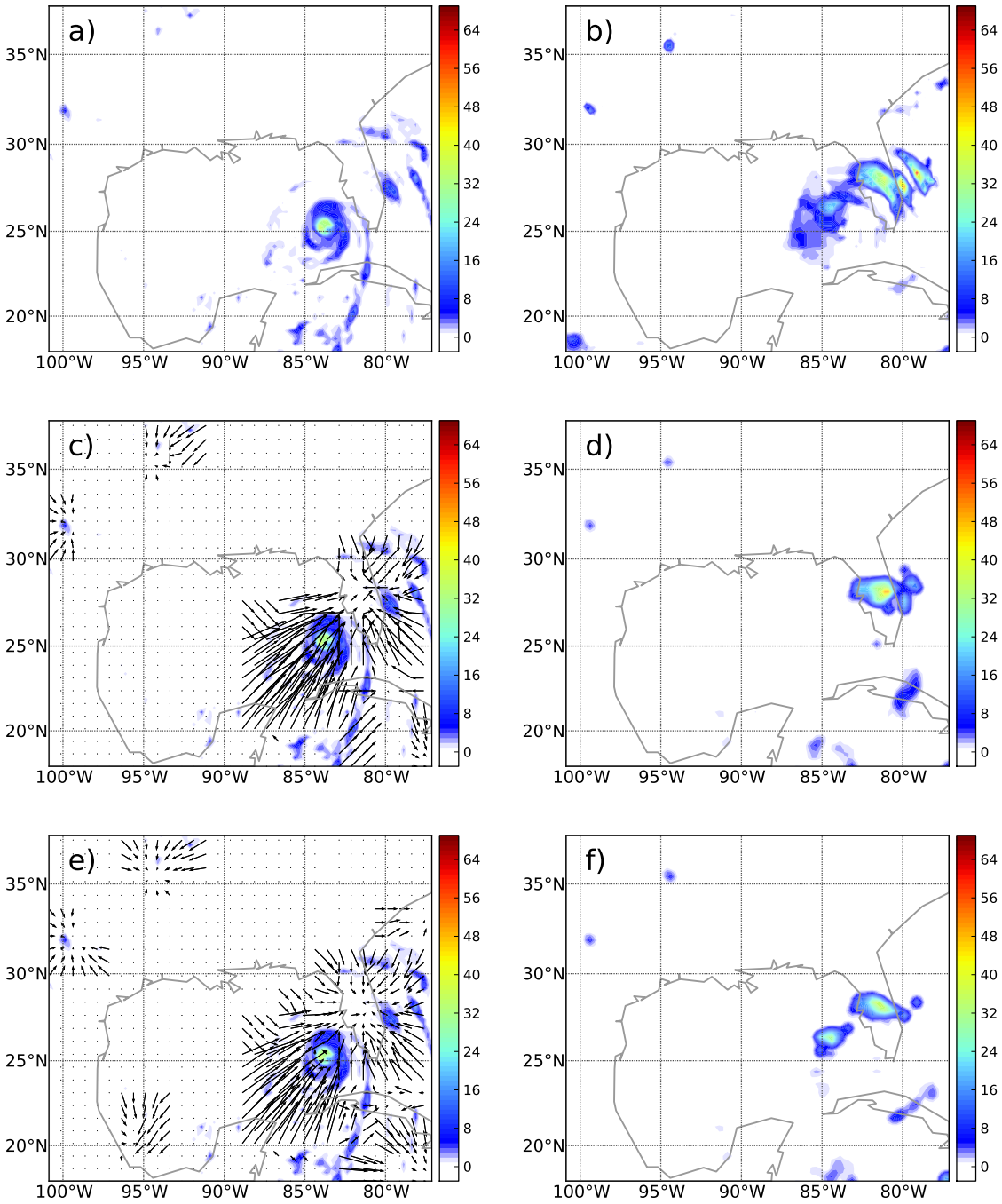

Figure 2.1: Illustration of the effect of modification of the pyramid matching algorithm. Shown are a) the forecast field, b) the verifying analysis, c) the optical flow for the original algorithm, d) the morphed field for the original algorithm, e) the optical flow for the modified algorithm and f) the morphed field for the modified algorithm.

3. DEFINITION OF THE ERROR COMPONENTS

While Keil and Craig [8, 9] defined the displacement error by the *mean magnitude* of the displacement vectors, we define it by the *magnitude of the mean* displacement vector. We also add the condition that the entire forecast feature must fall into the domain that the morphing can affect for the selected value of the subsampling parameter F. If no such forecast feature can be found, we say that the forecast has not captured the observed feature. This condition is necessary to ensure that smaller value of the displacement error is always associated with a less severe displacement of the precipitation feature in the forecast. It should also be noted that this definition of the displacement error treat all precipitation patterns in the verification domain as parts of a single system.

Keil and Craig [8, 9] also defined a second error component, which they called the *amplitude error*, to quantify the errors that the morphing was unable to correct. We define a similar error component, but we call it the *residual error*, as an error in the amplitude (intensity) of the forecast precipitation is not the only source of this error. In particular, it also has a component that reflects uncorrectable errors in the structure of the forecast feature.

3.1 Displacement error

The displacement error of Keil and Craig [8], δ_{disp}, can be formally written as

$$\delta_{disp} = \frac{1}{n} \sum_{i=1}^{N} \sum_{j=1}^{N} \left| d\mathbf{X}_{i,j} \right| . \tag{3.1}$$

Here, $n = n_1 + n_2$, where n_1 is the number of elementary parcels for which the displacement vector is nonzero and n_2 is the number of elementary parcels for which

the displacement vector is zero, but where the precipitation is nonzero (or larger than a small threshold) in both the original (un-morphed) forecast and the observation.

A problematic aspect of this definition is that the displacement vectors are, in general, not divergence- or rotation-free. Thus the average magnitude includes information, not only about the the displacement (translation) of the precipitation field in the forecast, but also about the corrections that are made by morphing to correct for errors in the structure of the precipitation field. The contribution of the divergent and the rotational component of the displacement vectors can be filtered from the measure of the displacement error by changing its definition to

$$\delta_{disp} = |d\mathbf{X}_{mean}| \tag{3.2}$$

where

$$d\mathbf{X}_{mean} = \frac{1}{n} \sum_{i=1}^{N} \sum_{j=1}^{N} d\mathbf{X}_{i,j}. \tag{3.3}$$

is the mean of the displacement vectors.

The definition of the displacement error is not complete, yet, because the metrics δ_{disp} defined by Eq. (3.3) leads to misleading results in situations where only part of the forecast precipitation pattern is sufficiently close to the observed pattern to be affected by morphing. To illustrate this problem, we consider an idealized test case, in which the verification domain consists of 24-by-24 elementary parcels and a uniform precipitation field that consists of 8-by-8 elementary parcels (Fig 3.1). The observed precipitation field (bottom right panel) is in the lower left corner of the verification domain. The displacement of the forecast precipitation field is gradually increased: in step k of the experiment, the "center of mass" of the forecast precipitation field is shifted by a distance of $k \times d$ compared to the "center of mass" of the observed

field. We carry out morphing experiments and compute δ_{disp} for $k = 1, 2, \ldots, 16$. (The top left and right panels of Fig 3.3 show the forecast precipitation field and the displacement vectors for $k = 5$.)

Our choice of the subsampling parameter is $F = 3$, that is, the pyramid has $F + 1 = 4$ levels. Figure 3.2 shows the values of δ_{disp} for the different values of k. In the parameter range from $k = 0$ to $k = 8$, δ_{disp} correctly indicates that the displacement error is $\sqrt{2}kd$. In the parameter range from $k = 9$ to $k = 16$, however, δ_{disp} indicates, incorrectly, that the displacement error decreases as the displacement of the forecast precipitation field increases. This pathological behavior of the measure occurs, because the morphing cannot move an elementary parcel, whose displacement is larger than $k = 2^F = 8$ in either direction. For those elementary parcels, the displacement vectors are zero vectors. As the displacement increases beyond $k = 2^F$ in either direction, an increasing number of displacement vectors become zero vectors, leading to a decrease of δ_{disp}. This argument shows that Eq. (3.3) provides a proper measure of the displacement error, only if the displacement of the forecast precipitation pattern is such that each of the elementary pixels in the pattern satisfies the condition that it is not separated by more than $2^F d$ elementary pixel from the closest elementary pixel of the observed precipitation feature. If no forecast precipitation feature is found that would satisfy this condition, it should be declared that none of the forecast features matches the observed feature.

The simplest approach to verify that the aforementioned condition is satisfied is to subject the morphed field to a visual inspection: if only part of a precipitation feature is affected by the morphing, the condition is not satisfied. The verification of the condition can also be automated, for example, by investigating the precipitation amounts in the elementary pixels located next to the most distant pixel that is still affected by the morphing.

3.2 Residual error

We define the residual error δ_{res} by the root-mean-square of the difference between the morphed forecast precipitation feature and the observed precipitation feature, that is, by

$$\delta_{res} = \left[\frac{1}{n} \sum_{i=1}^{N} \sum_{j=1}^{N} \left(P_{i,j}^{mf} - P_{i,j}^{a} \right)^2 \right]^{1/2}. \tag{3.4}$$

The square of the residual error can be decomposed as

$$\delta_{res}^2 = \delta_{int}^2 + \delta_{str}^2, \tag{3.5}$$

where δ_{int}^2 is the intensity error, which is defined by

$$\delta_{int} = \frac{1}{n} \sum_{i=1}^{N} \sum_{j=1}^{N} \left(P_{i,j}^{mf} - P_{i,j}^{a} \right), \tag{3.6}$$

and δ_{str}^2 is the part of the structure error that cannot be corrected by morphing and is defined by

$$\delta_{str} = \left[\frac{1}{n} \sum_{i=1}^{N} \sum_{j=1}^{N} \left(P_{i,j}^{mf} - P_{i,j}^{a} - \delta_{int} \right)^2 \right]^{1/2}. \tag{3.7}$$

The structure error measures the magnitude of the component of the forecast error that cannot be corrected by morphing.

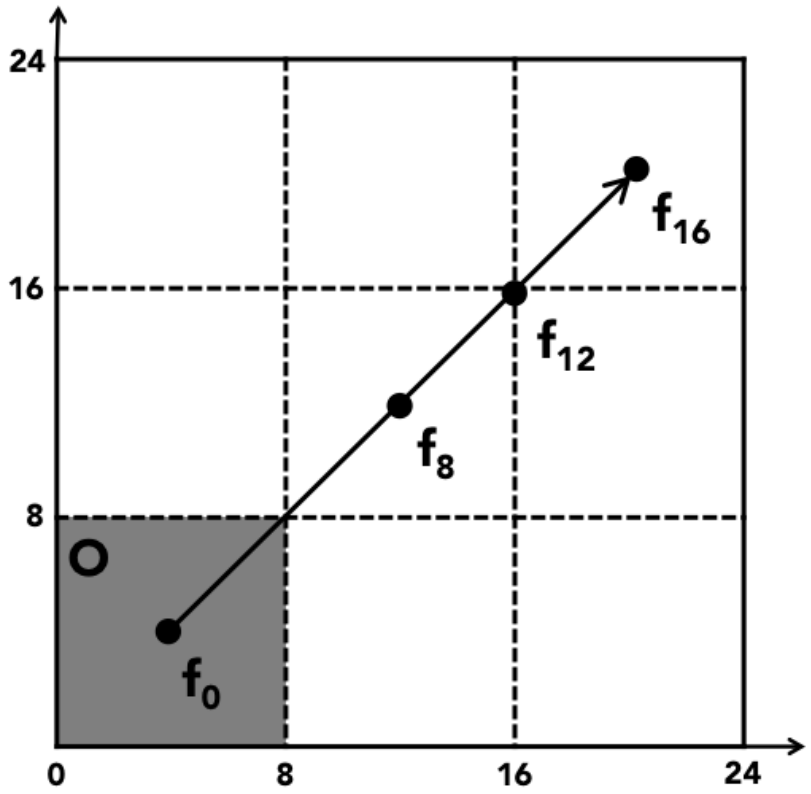

Figure 3.1: Schematic illustration of the idealized case considered in Sec. 2.a. The full domain consists of 24×24 elementary pixels. The forecast and observed features consist of 8×8.The observed feature (square filled with dark grey shade) is located in the lower left corner, while the forecast feature is gradually shifted along the main diagonal in the direction indicated by the arrow. The dots at locations f_k, $k = 1, 8, 12, 16$ along the diagonal indicate the center of the forecast feature in the case where the forecast feature is displace by k positions in both directions.

i

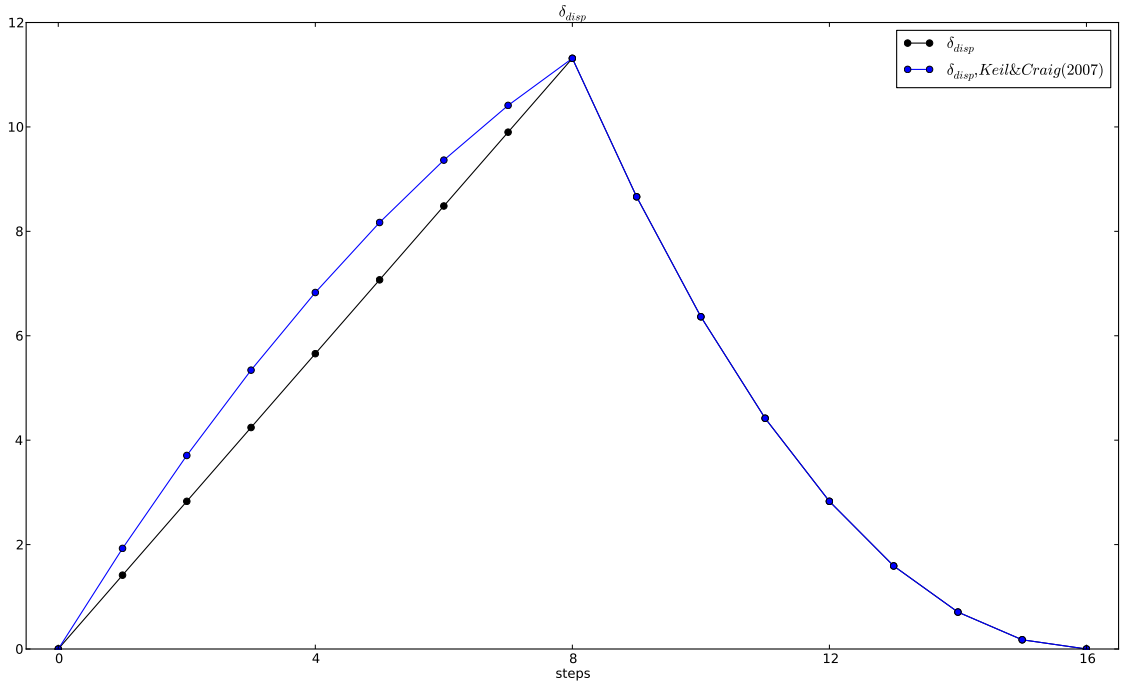

Figure 3.2: The value of the displacement error computed for the schematic example of Fig. 3.1 by Eq. (3.1) (blue) and Eq. (3.2) (black). For $k > 8$, the two curves overlap.

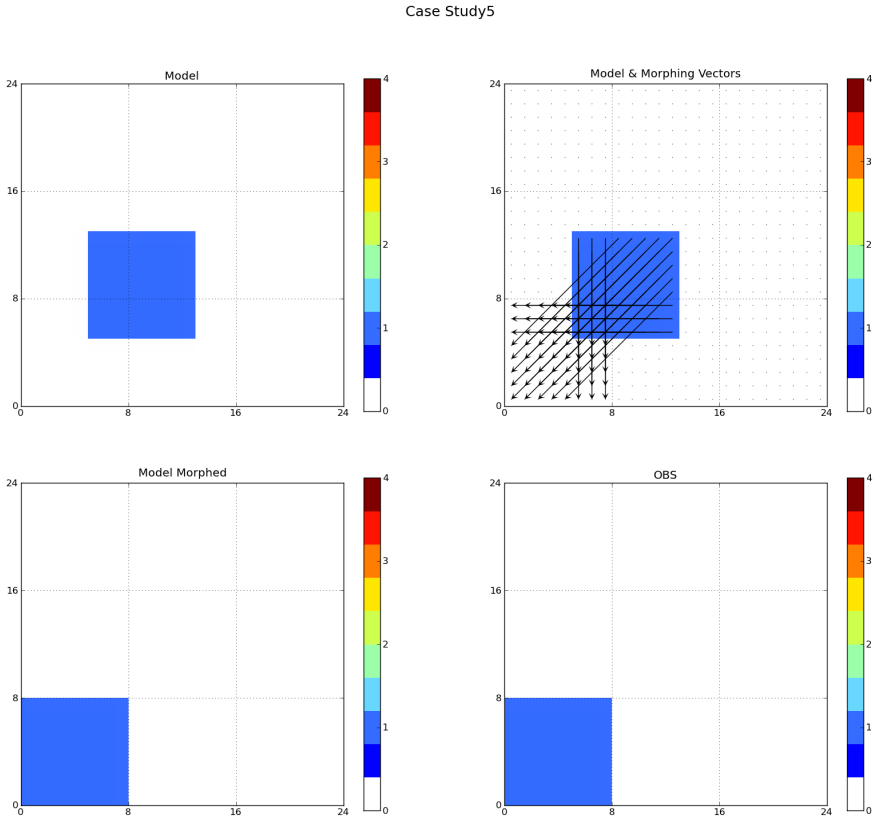

Figure 3.3: Illustration of the morphing for the schematic example of Fig. 3.1. Shown are (top left) the forecast feature, (bottom right) the observed feature, (top right) the optical flow with the forecast feature underlaid and (bottom left) the morphed forecast feature.

4. APPLICATION TO FORECASTS OF HURRICANE ISAAC

We demonstrate the behavior of he proposed morphing-based verification scores in a realistic scenario by computing them for high-resolution forecasts of hurricane Isaac. Traditional precipitation verification scores, the equitable threat score (ETS) and root-mean-square (RMS) error, are also computed for comparison.

4.1 Forecast data

The forecasts we verify were produced in real time by the Coupled Regional Climate Model (CRCM) of Texas A&M University. The CRCM is a coupled version of the Advanced Research WRF (WRF-ARW) community atmospheric model and the Regional Ocean Model System (ROMS) community ocean model. Earlier versions of the model have been used in a series of studies [e.g., 13, 14]. The version of the model that produced the 3 km horizontal resolution forecasts that we use in our example is described in Ma et al. [11]. The initial and the boundary conditions of the model runs were provided by the operational North American Mesoscale (NAM) analyses for the atmosphere component and the Real-Time Ocean Forecast System (RTOFS) analyses for the ocean component.

4.2 Verification data

For the verification of the forecasts, we use retrievals and analyses rather than observations. In particular, we combine the TRMM 3B42 (Version 7) three-hourly, $0.25^o \times 0.25^o$ retrieval product of NASA and the Stage IV precipitation analysis product of the National Centers for Environmental Prediction (NCEP).

The TRMM 3B42 (Version 7) retrievals are based on microwave (MW) observations where such observations are available and infrared (IR) observations where MW

observations are not available [7]. The retrievals are more reliable over ocean than land, because observations can be used from more channels over oceans, where the difference between the emissivity of the surface and the emissivity of the precipitating clouds is larger [1].

The Stage IV analysis is a multi-sensor (radar and gauge) precipitation analysis over the United States. Stage IV precipitation estimates are produced by combining data from several Weather Surveillance Radar-1099 Doppler (WSR-88D) radars with real-time surface rain gauge observations [10]. The estimates are available as hourly rainfall accumulations for approximately 4 km×4 km pixels. (The area covered by the Stage IV precipitation analysis is shown in Fig 4.1).

To take advantage of the full coverage of the model domain by TRMM 3B42's retrievals and the higher accuracy of the Stage IV analysis over land, we combine the two data sets into a single verification data set by the following procedure:

1. The data for the CRCM forecast domain is extracted from both the TRMM 3B42 and the Stage IV data sets.

2. The coarser-resolution forecast and Stage IV datasets are interpolated to the resolution of the TRMM 3B42 grid by using an area-mean interpolation to conserve total precipitation.

3. A time averaging is applied to both the forecast and the Stage IV and forecast datasets to match the 3 h intervals for which the TRMM 3B42 data are available.

4. The TRMM 3B42 data are replaced by the re-gridded Stage IV data wherever they are available.

4.3 Equitable threat score (ETS) and root-mean-square (RMS) error

Both the forecast and the verification precipitation fields are replaced by fields of 1's and 0's, where 1 and 0 indicate precipitation locations with precipitation over a prescribed threshold and no precipitation over the same threshold, respectively. Then, a 2*2 contingency table is prepare with the counts of four mutually exclusive and collectively exhausive events: (a) the number of locations of 'hits', that is, the number of locations where the binary value is 1 in both the forecast and the verification fields'; (b) the number of locations of 'misses', that is, the number of locations where the binary value is 0 in the forecast field, but 1 in the verification field; (c) the number of locations of 'false alarms', that is, the number of locations where the binary value is 1 in the forecast field, but 0 in the verification field; and (d) the number of locations of 'correct negatives', that is, the number of locations where the binary value is 0 in both the forecast and the verification fields. By using a certain threshold, the above contingency table counts are generated for each 3-hourly precipitation over the forecast domain.

The ETS is then defined by

$$ETS = \frac{hits - hits_{random}}{hits + misses + false\,alarms - hits_{random}} \tag{4.1}$$

where $hits_{random}$ is the number of hits associated with random chance. It is defined by

$$hits_{random} = \frac{(hits + misses)(hits + false\,alarms)}{hits + misses + false\,alarms + correct\,negtives} \tag{4.2}$$

ETS ranges from $-\frac{1}{3}$ (complete mismatch) to 1 (perfect match). For a random forecast fields, the value of ETS is zero.

The root-mean-square (RMS) error is defined by

$$RMS = \left[\frac{1}{N^2} \sum_{i=1}^{N} \sum_{j=1}^{N} \left(P_{i,j}^{m} - P_{i,j}^{a} \right)^2 \right]^{1/2} . \tag{4.3}$$

Here $P_{i,j}^{f}$ is the forecast amount of precipitation at grid point i, j, and $P_{i,j}^{a}$ is the observed amount of precitation at grid point i, j.

4.4 Hurricane Isaac

Our focus is on the time period from 0500 UTC 26 August 2012 to 0500 UTC 4 September 2012. Hurricane Isaac entered the Gulf of Mexico, heading northwest, at the beginning of this period. It later intensified and became a Category 2 hurricane just before making landfall near the mouth of the Mississippi River at 0445 UTC on 29 August 2012. It caused a relatively large storm surge and produced heavy precipitation. It weakend into a tropical storm at around 1900 UTC on August 29 as it was slowly moving through Louisiana. It continued its northeastward movement over northern Louisiana, Arkansas and Missouri and at around 2100 UTC on August 30, its was degraded to a tropical depression. On September 1, the storm transitioned into an extratropical cyclone after interacting with an eastward propagating upper-level trough.

The main body of Isaac moved out of the CRCM forecast domain on August 31. The forecast data we examine are from seven forecast run started at 0500 UTC each day from August 26th to September 1st. We examined each forecast at 24 different forecast times (every three hours up to the 72 h forecast time) and selected three representative cases to describe here.

4.5 Verification results

We choose the parameters of the pyramid matching algorithm as follows:

1. To filter the large areas of light rain, which are model artifacts, forecast values of precipitation that are smaller than 1 mm/h are replaced by 0 mm/h.

2. The subsampling factor is $F = 3$. That is, the search distance for the top pyramid level is $0.25^{\circ} \times 2^F = 2^{\circ}$ in both the zonal and the meridional directions.

3. The local hit rate threshold is $\varepsilon = 0.5$.

The values of the different verification scores for the cases investigated here are listed in Table 4.1. For comparison, the table also includes the values of the equitable threat score (ETS) and the root-mean-square (RMS) error for each case.

Fig 4.2 shows the effect of morphing for the 42 h forecast started at 0500 UTC August 26th. The main precipitation pattern associated with the storm is displaced by about 2° in the northeast direction in the forecast, while the outer rain band east of Florida is shifted by about 2° in the southwest direction. According to ETS, the forecast has almost no skill and the RMS error is also large. As for the morphing-based measures, the displacement error is $\delta_{disp} = 2.773^{\circ}$. The residual error ($\delta_{res} = 0.942$) is much smaller than the RMS error (2.068), which indicates that morphing is highly efficient in this case. The intensity error component of the residual error is much smaller ($\delta_{int} = 0.017$) than the structural error component ($\delta_{str} = 0.941$), which suggests that the error that the morphing cannot correct is primarily due to errors in the structure of the prediction of the flow rather than to an error in the prediction of the total precipitation associated with the hurricane.

To investigate whether our definition of the displacement error leads to a more realistic description of the displacement of the precipitation system in the forecast that the measure introduced by Keil and Craig [8], we also compute the measure of the displacement error by Eq. (3.1). We denote the latter measure by $\delta_{disp,KC}$, which has a value ($\delta_{disp,KC} = 8.606^{\circ}$) much larger than that obtained by Eq. (3.2). If the

Table 4.1: Summary of the verification scores for the examples of Sec. 4.

Case No.	$\delta_{disp}\ (deg)$	$\delta_{disp,KC}\ (deg)$	RMS	ETS	δ_{res}	δ_{int}	δ_{str}
$Aug.26, +42\ h$	2.773°	8.606°	2.068 mm	0.025	0.942 mm	0.001 mm	0.941 mm
$Aug.29, +27\ h$	3.073°	6.238°	1.927 mm	0.078	1.287 mm	0.080 mm	1.285 mm
$Aug.29, +54\ h$	4.801°	5.551°	2.251 mm	0.018	1.267 mm	0.178 mm	1.256 mm

entire precipitation system of the hurricane is considered a single forecast feature, Eq. (3.2) provides an obviously more accurate description of its displacement in the forecast than Eq. (3.1).

Figures 4.3 and 4.4 illustrate the effects of morphing by two more cases. For the forecast shown Fig 4.3, the conclusions are very similar to those for Fig 4.2. The case shown in Fig 4.4 is different from the other two in that Eq. (3.2) and Eq. (3.1) provide more similar estimates of the displacement error. This result is due to the property of the optical flow, which can be easily seen by visually inspecting Fig 4.4, that the divergent and the rotational components of the flow are weak.

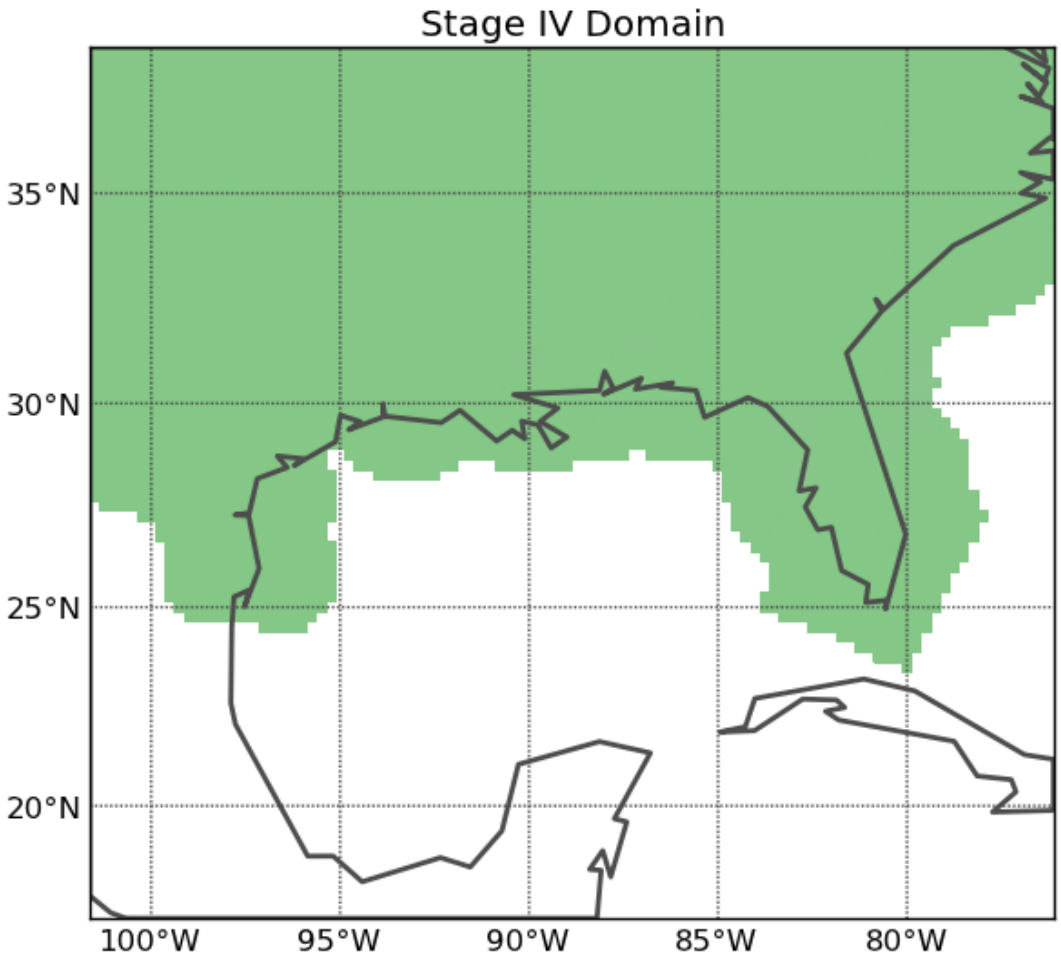

Figure 4.1: Illustration of the NCEP Stage IV analysis data coverage. The region for which NCEP Stage IV analyses are available are indicated by green shades.

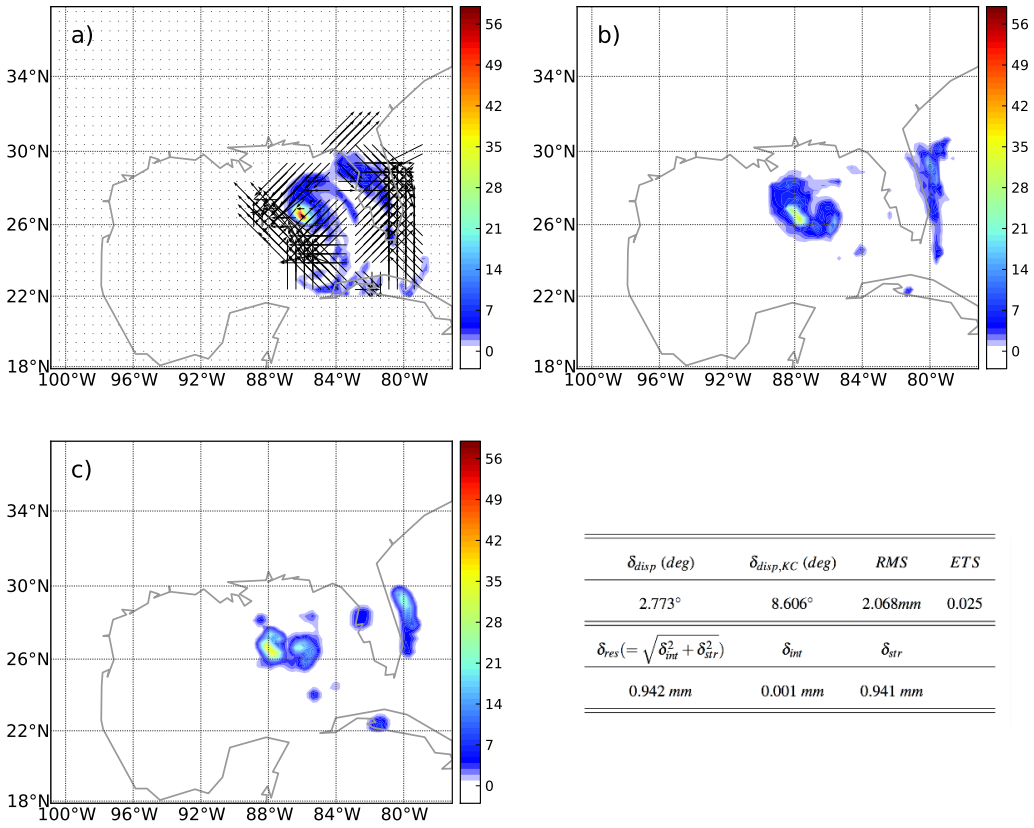

δ_{disp} (deg)	$\delta_{disp,KC}$ (deg)	RMS	ETS
2.773°	8.606°	2.068mm	0.025
$\delta_{res}(=\sqrt{\delta_{int}^2+\delta_{str}^2})$	δ_{int}	δ_{str}	
0.942 mm	0.001 mm	0.941 mm	

Figure 4.2: Illustration of the morphing and error measures for the 42 h forecast started on 26 August. Shown are a) the forecast field and the optical flow, b) the verification field and c) the morphed field.

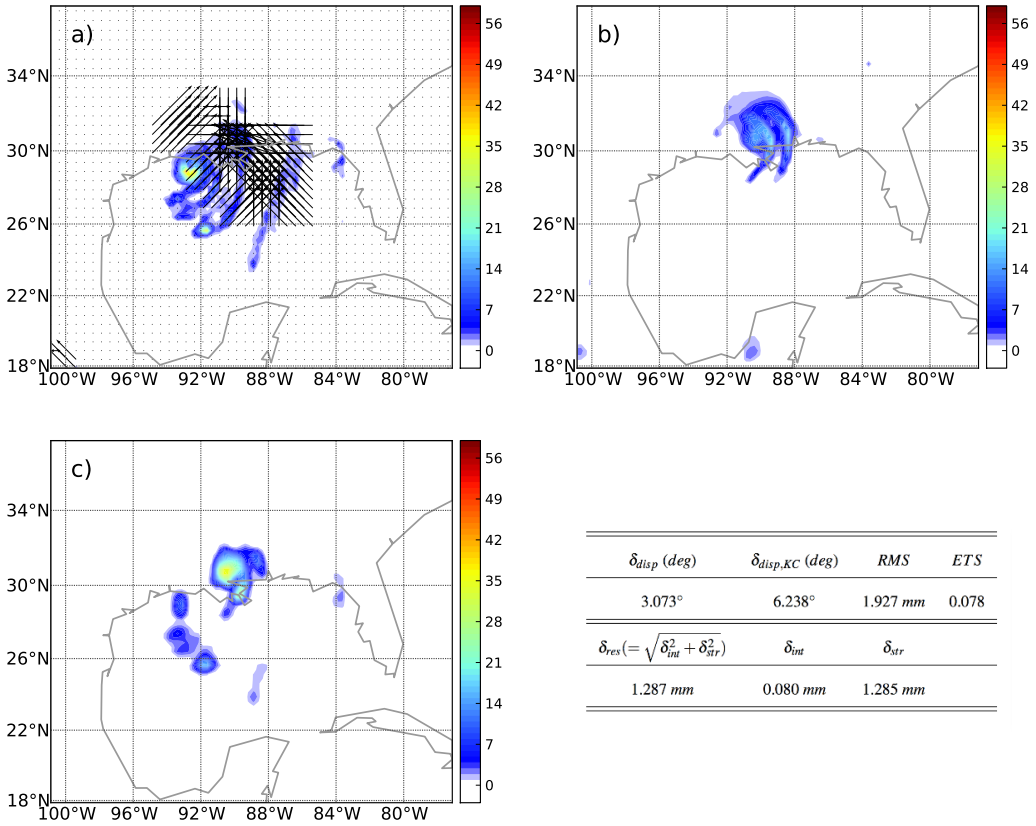

δ_{disp} (deg)	$\delta_{disp,KC}$ (deg)	RMS	ETS
3.073°	6.238°	1.927 mm	0.078
$\delta_{res}(=\sqrt{\delta_{int}^2+\delta_{str}^2})$	δ_{int}	δ_{str}	
1.287 mm	0.080 mm	1.285 mm	

Figure 4.3: Same as Fig. 4.2, but for the 27-h forecast started on 29 August.

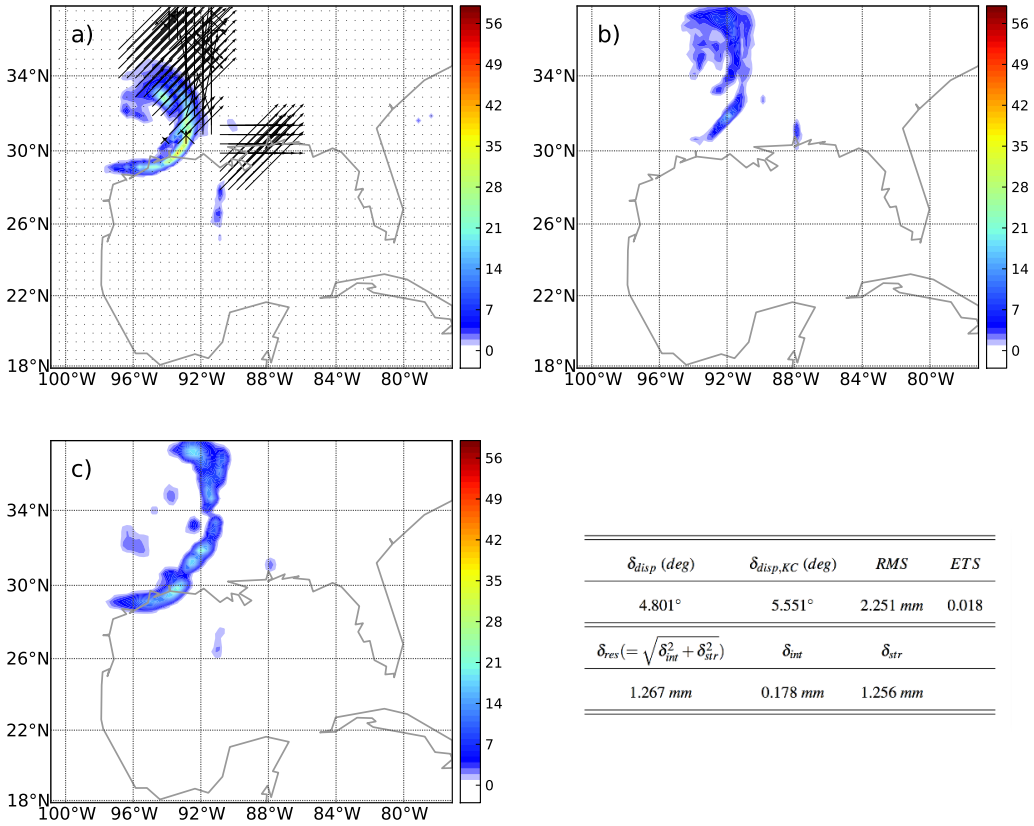

δ_{disp} (deg)	$\delta_{disp,KC}$ (deg)	RMS	ETS
4.801°	5.551°	2.251 mm	0.018
$\delta_{res}(=\sqrt{\delta_{int}^2+\delta_{str}^2})$	δ_{int}	δ_{str}	
1.267 mm	0.178 mm	1.256 mm	

Figure 4.4: Same as Fig. 4.2, but for the 54-h forecast started on 29 August.

5. CONCLUSIONS

In this paper, we described a morphing-based precipitation verification strategy. This strategy was inspired by the pair of papers Keil and Craig [8, 9]. The novel aspects of our strategy is that

- it imposes a constraint on morphing in order to prevent the over-convergence of pixels during morphing to a few locations of large errors; and
- it uses a new definition of the displacement error and also provides a new interpretation of the other terms.

We illustrated the advantageous properties of the modified morphing algorithm and the new definition of the error term by both schematic and realistic examples.

REFERENCES

[1] Y. Chen, E. E. Ebert, K. J. E. Walsh, and N. E. Davidson. Evaluation of TRMM 3B42 precipitation estimates of tropical cyclone rainfall using pacrain data. *J. Geophys. Res.: Atmospheres*, 2013.

[2] C. Davis, B. Brown, and R. Bullock. Object-based verification of precipitation forecasts. part I: Methodology and application to mesoscale rain areas. *Mon. Wea. Rev.*, 134(7):1772–1784, 2006.

[3] J. Done, C. A. Davis, and M. Weisman. The next generation of NWP: Explicit forecasts of convection using the weather research and forecasting (WRF) model. *Atmos. Sci. Let.*, 5(6):110–117, 2004.

[4] E. E. Ebert. Neighborhood verification: A strategy for rewarding close forecasts. *Wea. and Forecasting*, 24(6):1498–1510, 2009.

[5] E. E. Ebert and J. L. McBride. Verification of precipitation in weather systems: Determination of systematic errors. *J. Hydrol.*, 239(1):179–202, 2000.

[6] E. Gilleland, D. Ahijevych, B. G. Brown, B. Casati, and E. E. Ebert. Intercomparison of spatial forecast verification methods. *Wea. and Forecasting*, 24(5): 1416–1430, 2009.

[7] G. J. Huffman, D. T Bolvin, E. J. Nelkin, D. B. Wolff, R. F. Adler, G. Gu, Y. Hong, K. P. Bowman, and E. F. Stocker. The TRMM multisatellite precipitation analysis (TMPA): Quasi-global, multiyear, combined-sensor precipitation estimates at fine scales. *J. Hydrometeor.*, 8(1):38–55, 2007.

[8] C. Keil and G. C. Craig. A displacement-based error measure applied in a regional ensemble forecasting system. *Mon. Wea. Rev.*, 135(9):3248–3259, 2007.

[9] C. Keil and G. C. Craig. A displacement and amplitude score employing an

optical flow technique. *Wea. and Forecasting*, 24(5):1297–1308, 2009.

[10] Y. Lin and K. E. Mitchell. 1.2 the NCEP Stage II/IV hourly precipitation analyses: development and applications. 2005. URL `https://ams.confex.com/ams/pdfpapers/83847.pdf`.

[11] X. Ma, P. Chang, R. Saravanan, R. Montuoro, J. Hsieh, D. Wu, X. Lin, and L. Wu. Ocean meso-scale eddies influencing weather patterns in the North Pacific. *Nature Geoscience*, page under review, 2014.

[12] C. F. Mass, D. Ovens, K. Westrick, and B. A. Colle. Does increasing horizontal resolution produce more skillful forecasts? *Bull. Amer. Meteor. Soc.*, 83(3): 407–430, 2002.

[13] C. M. Patricola, M. Li, Z. Xu, P. Chang, R. Saravanan, and J.-S. Hsieh. An investigation of tropical Atlantic bias in a high-resolution coupled regional climate model. *Clim. Dyn.*, 39:2443–2463, 2012.

[14] C. M. Patricola, R. Saravanan, and P. Chang. The impact of the El Nino-Southern Oscillation and Atlantic meridional mode on seasonal Atlantic tropical cyclone activity. *J. Climate*, 39:in press, 2014.

[15] R. Romero, C.A. Doswell III, and R. Riosalido. Observations and fine-grid simulations of a convective outbreak in northeastern Spain: Importance of diurnal forcing and convective cold pools. *Mon. Wea. Rev.*, 129(9):2157–2182, 2001.

[16] M. S. Speer and L. M. Leslie. The prediction of two cases of severe convection: implications for forecast guidance. *Meteorol. Atmos. Phys.*, 80(1-4):165–175, 2002.

[17] M. L. Weisman, W. C. Skamarock, and J. B. Klemp. The resolution dependence of explicitly modeled convective systems. *Mon. Wea. Rev.*, 125(4):527–548, 1997.

[18] T. Zinner, H. Mannstein, and A. Tafferner. Cb-TRAM: Tracking and monitoring severe convection from onset over rapid development to mature phase using

multi-channel Meteosat-8 SEVIRI data. *Meteorol. Atmos. Phys.*, 101(3-4):191–210, 2008.